Theoretical analysis of mixing in liquid clouds. Part IV: DSD evolution and mixing diagrams

Mark Pinsky, and Alexander Khain

Department of Atmospheric Sciences, The Hebrew University of Jerusalem, Israel

Submitted to

Atmospheric Chemistry and Physics

May 2017

Revised September 2017

Second revision: November 2017

Final revision: January 2018

Communicating author: Alexander Khain, The Hebrew University of Jerusalem, khain@vms.huji.ac.il

Abstract

Evolution of droplet size distribution (DSD) due to mixing between cloudy and dry volumes is investigated for different values of the cloud fraction and for different initial DSD shapes. The analysis is performed using a diffusion-evaporation model which describes time-dependent processes of turbulent diffusion and droplet evaporation within a mixing volume. Time evolution of the DSD characteristics such as droplet concentration, LWC and mean volume radii is analyzed. The mixing diagrams are plotted for the final mixing stages. It is shown that the difference between the mixing diagrams for homogeneous and inhomogeneous mixing is insignificant and decreases with an increase in the DSD width. The dependencies of normalized cube of the mean volume radius on the cloud fraction were compared with those on normalized droplet concentration and found to be quite different. In case the normalized droplet concentration is used, mixing diagrams do not show any significant dependence on relative humidity in the dry volume.

The main conclusion of the study is that traditional mixing diagrams cannot serve as a reliable tool for analysis of mixing type.

Keywords: turbulent mixing, droplet evaporation, DSD evolution, mixing diagram

1. Introduction

The effects of mixing of cloudy air with surrounding dry air on cloud microphysics are still the focus of many studies (see overview by Devenish et al., 2012). Processes of mixing are investigated in observations (Yum et al., 2015; Bera at al., 2016a,b), Large Eddy Simulations (Andrejczuk et al., 2009; Khain et al., 2017) and Direct Numerical Simulations (Kumar et al., 2014, 2017). Processes of mixing and their effects on droplet size distributions were recently investigated in a set of theoretical studies (Yang et al., 2016; Korolev et al., 2016 (hereafter, Pt1); Pinsky et al., 2016 a,b).

The Pt1 presented analysis of conventional (classical) concept of mixing and introduced the main parameters characterizing homogeneous and extremely inhomogeneous mixing. In the classical concept two volumes, cloudy and droplet free one, mix within an unmovable adiabatic mixing volume. At a monodisperse initial droplet size distribution (DSD), homogeneous mixing leads to a decrease in droplet size and droplet mass content, while the number of droplets remains unchanged. Extremely inhomogeneous mixing is characterized by decreasing the number of droplets due to full evaporation of some fraction of droplets penetrating the initially dry air volume while the DSD shape in the cloud volume remains unchanged. As a result of extremely inhomogeneous mixing, droplet number decreases while the mean volume radii remain unchanged. At a polydisperse DSDs, the extreme homogeneous mixing is characterized by proportional changes in DSD for all droplet radii (Pt1). Since widely used mixing diagrams describe the final equilibrium stage of mixing within the mixing volume they do not contain information about changes in microphysical quantities in the course of mixing.

Pinsky et al. (2016a, hereafter Pt2) analyzed the time evolution of initially monodisperse and polydisperse DSD during homogeneous mixing. It was shown that result of mixing strongly depends on the shape of the initial DSD. At a wide DSD, evaporation of droplets (first of all, of the smallest ones) is not accompanied by a decrease in the mean volume or effective radius. Moreover, the values of the radii may even increase over time. This result

indicates that the widely used criterion of separation of mixing types based on the behavior of the mean volume radius during mixing is not generally relevant and may be wrong in application to real clouds.

Pinsky et.al. (2016b, hereafter Pt3) introduced a diffusion-evaporation model which describes evolution DSDs and all the microphysical variables due to two simultaneously occurring processes: turbulent diffusion and droplet evaporation. Mixing between two equal volumes of subsaturated and cloudy air was analyzed, i.e. it was assumed that the cloud volume fraction $\mu = 1/2$. The initial DSD in the cloudy volume was assumed monodisperse. These simplified assumptions allowed to reduce the turbulent mixing equations to two-parametric ones. The first parameter is the Damkölher number, Da, which is the ratio of the characteristic mixing time to the characteristic phase relaxation time. The second parameter is the potential evaporation parameter R characterizing the ratio between the amount of water vapor needed to saturate the initially dry volume and the amount of available liquid water in the cloudy volume.

Within the $Da - R$ space, in addition to the two extreme mixing types defined in the classical concept, two more mixing regimes were distinguished, namely, intermediate and inhomogeneous mixing. It was shown that any type of mixing leads to formation of a tail of small droplets, i.e. to DSD broadening. It was also shown that the relative humidity in the initially dry volume rapidly increases due to both water vapor diffusion and evaporation of penetrating droplets. As a result, the mean volume and effectice radii in the initially dry volume rapidly approach the values typical of cloudy volume. At the same time, the liquid water content (LWC) remains significantly lower than that in the cloudy volume during much longer time than required for the effective droplet radius to grow.

In the present study (Pt4) we continue investigating the turbulent mixing between an initially droplet free volume (referred to as dry volume) and a cloudy volume. The focus of the study is investigation of DSD temporal evolution and analysis of the final equilibrium

DSD. In comparison to Pt3, the problem analyzed in this study is more sophisticated in several aspects:

- The dependences of different mixing characteristics on cloud volume fraction $0 \le \mu \le 1$ are analyzed. In this case the equations of turbulent mixing cannot be reduced to the two-parametric problem as it was done in Pt3.
- The initial DSDs in cloud volume are polydisperse. We use both narrow and wide initial DSD described by Gamma distributions with different sets of parameters. The DSD are the same as those used in Pt2. Mechanisms of formation of wide DSDs in clouds including DSDs in undiluted cloud cores were investigated in several studies [e.g., Khain et al., 2000; Pinky and Khain, 2002; Segal et al., 2004; Prabha et al., 2011]. These studies show the DSD broadening is caused by in-cloud nucleation of droplets within clouds as well as by collisions between cloud droplets. It was shown that DSDs in adiabatic volumes can be wide and first raindrops or drizzle drop arise namely in non-diluted adiabatic cloud parcels [Khain et al., 2013; Magaritz-Ronen et al., 2016]. We use both narrow and wide DSDs in the form of Gamma distribution with typical parameters used in different cloud resolving models. The DSDs that are used as initial ones in cloudy volumes could be formed also under influence of mixing during their previous history. The mechanisms of the formation of initial DSD are not of interest in the study since that do not affect the analysis.
- The equation for supersaturation, used in this study, is valid at low humidity in the initially dry volume and is more general and compared with that used in Pt3, which makes the DSD calculations more accurate.

At the same time, some simplifications used in Pt3 are retained in this study. The vertical movement of the entire mixing volume is neglected; collisions between droplets and droplet sedimentation are not allowed. Also, we consider a 1D diffusion-evaporation problem. We neglect the changes of temperature in the course of mixing, which is possibly a less significant

simplification. All these simplifications allow to reveal the effects of turbulent mixing and evaporation on DSD evolution.

2. Formulation of the problem and model design

In this study, the process of mixing is investigated basing on the solution of 1D diffusion-evaporation equation (see also Pt3). According to this equation, evaporation of droplets due to negative supersaturation in the mixing volume takes place simultaneously with turbulent mixing. Since droplets within the volume are under different negative supersaturation values until the final equilibrium is reached, the modeled mixing is inhomogeneous. The droplets can evaporate either partially or totally. The evaporation leads to a decrease in droplet sizes and in droplet concentration.

Like in Pt3, the process of turbulent diffusion is described by a 1D equation of turbulent diffusion. The equation does not describe formation of separate turbulent filaments. Instead, it describes averaged effects of turbulent vortices of different scales by modeling of turbulent diffusion, characterized by a typical value of turbulent diffusion coefficient K. The mixing is assumed to be driven by isotropic turbulence at scales within the inertial sub-range where Richardson's law is valid. In this case, turbulent coefficient is evaluated as in Monin and Yaglom (1975):

$$K(L) = C\varepsilon^{1/3}L^{4/3} \quad (1)$$

In Eq. (1) ε is the turbulent kinetic energy dissipation rate and $C = 0.2$ is a constant (Monin and Yaglom, 1975), Boffetta and Sokolov (2002). Eq. (1) means that we consider the effects of turbulent diffusion at scales much larger than the Kolmogorov microscale, i.e. the effects of molecular diffusion are neglected. In the simulations, we use $L = 40\ m$ and $\varepsilon = 20 cm^2 s^{-3}$. It means that in the present study mixing is performed by vortices smaller than several tens of meters which agrees with measurements in warm Cu (Gerber et al. 2008). The value of turbulent kinetic energy dissipation rate chosen is also typical for small Cu (e.g. Gerber et al.

2008). These parameters correspond to the values of Da of several hundred. The model allows utilization of other values of L and ε typical of other cloud type (say, deep convective clouds) which can change results quantitatively, but not qualitatively.

Geometry of mixing and the initial conditions

The conceptual scheme presenting mixing geometry and the initial conditions used in the following analysis are shown in **Figure 1**.

Fig 1 here

At $t = 0$ the mixing volume of length L is divided into two volumes: the cloud volume of length μL (Fig.1, left) and the dry volume of length $(1-\mu)L$ (Fig.1, right), where $0 \le \mu \le 1$ is the cloud volume fraction. The entire volume is assumed closed, i.e. adiabatic. At $t = 0$ the cloud volume is assumed saturated, so the supersaturation $S_1 = 0$. This volume is also characterized by the initial distribution of the square of the droplet radii $g_1(\sigma)$, where $\sigma = r^2$. The initial liquid water mixing ratio in the cloudy volume is equal to $q_{w1} = \frac{4\pi\rho_w}{3\rho_a}\int_0^\infty \sigma^{3/2} g_1(\sigma) d\sigma$. The integral of $g_1(\sigma)$ over σ is equal to the initial droplet concentration in the cloud volume $N_1 = \int_0^\infty g_1(\sigma) d\sigma$. The initial droplet concentration in the dry volume is $N_2 = 0$, the initial negative supersaturation in this volume is $S_2 < 0$ and the initial liquid water mixing ratio $q_{w2} = 0$. Therefore, the initial profiles of these quantities along the x-axis are step functions:

$$N(x,0) = \begin{cases} N_1 & \text{if} \quad 0 \le x < \mu L \\ 0 & \text{if} \quad \mu L \le x < L \end{cases} \qquad (2a)$$

$$S(x,0)=\begin{cases}0 & \text{if} \quad 0\le x<\mu L\\ S_2 & \text{if} \quad \mu L\le x<L\end{cases} \tag{2b}$$

$$q_w(x,0)=\begin{cases}q_{w1} & \text{if} \quad 0\le x<\mu L\\ 0 & \text{if} \quad \mu L\le x<L\end{cases} \tag{2c}$$

The initial profile of droplet concentration is shown in Fig. 1b. This is the simplest inhomogeneous mixing scheme, wherein mixing takes place only in the x-direction, and the vertical velocity is neglected.

Since the total volume is adiabatic, the fluxes of different quantities through the left and right boundaries at any time instance are equal to zero, i.e.

$$\frac{\partial N(0,t)}{\partial x}=\frac{\partial N(L,t)}{\partial x}=0;\ \frac{\partial q_w(0,t)}{\partial x}=\frac{\partial q_w(L,t)}{\partial x}=0;\frac{\partial q_v(0,t)}{\partial x}=\frac{\partial q_v(L,t)}{\partial x}=0 \tag{3}$$

where q_v is the water vapor mixing ratio.

To investigate of mixing process for different initial DSD, we assume that DSD in the cloud volume can be represented by a Gamma distribution:

$$f\ (r,t=0)=\frac{N_0}{\Gamma(\alpha)\beta}\left(\frac{r}{\beta}\right)^{\alpha-1}\exp\left(-\frac{r}{\beta}\right) \tag{4}$$

where N_0 is an intercept parameter, α is a shape parameter and β is a slope parameter of distribution. The DSD $f\ (r)$ relates to distribution $g_1(\sigma)$ as $f(r)=2rg_1(\sigma)$. We performed simulations with both initially wide and narrow DSDs. The width of DSD is determined by a set of parameters. The parameters of the initial Gamma distributions used in this study are presented in **Table 1**. Parameters of the distributions are chosen in such a way that the modal radii of DSD and the values of LWC are the same for both distributions. These distributions were used in Pt2 for analysis of homogeneous mixing.

Table 1 here

196

197

198 ***Conservative quantity*** $\Gamma(x,t)$

199 The supersaturation equation for an adiabatic immovable volume can be written in the

200 form $\frac{1}{S+1}\frac{dS}{dt} = -A_2 \frac{dq_w}{dt}$, where S is supersaturation over water, and the coefficient

201 $A_2 = \frac{1}{q_v} + \frac{L_w^2}{c_p R_v T^2}$ is slightly dependent on temperature (Korolev and Mazin, 2003) (notations

202 of other variables are presented in **Appendix**). In our analysis we consider A_2 to be a

203 constant. As follows from the supersaturation equation, the quantity

204

205 $$\Gamma(x,t) = \ln\left[S(x,t)+1\right] + A_2 q_w(x,t) \qquad (5)$$

206

207 is a conservative quantity, i.e. it is invariant with respect to phase transitions. In Eq. (5),

208 $|S(x,t)|$ can be comparable with unity by the order of magnitude. The conservative quantity

209 $\Gamma(x,t)$ obeys the following equation for turbulent diffusion

210

211 $$\frac{\partial \Gamma(x,t)}{\partial t} = K \frac{\partial^2 \Gamma(x,t)}{\partial x^2} \qquad (6)$$

212

213 with the adiabatic (no flux) condition at the left and right boundaries $\frac{\partial \Gamma(0,t)}{\partial x} = \frac{\partial \Gamma(L,t)}{\partial x} = 0$

214 and the initial profile at $t = 0$

215

216 $$\Gamma(x,0) = \begin{cases} A_2 q_{w1} & \text{if} \quad 0 \le x < \mu L \\ \ln\left[S_2 + 1\right] & \text{if} \quad \mu L \le x < L \end{cases} \qquad (7)$$

217

From Eq. (7) it follows that $\Gamma(x,0)$ is positive in the cloud volume and negative in the initially dry volume. The mean value of function $\Gamma(x,0)$ can be written as follows:

$$\bar{\Gamma} = \frac{1}{L}\int_0^L \Gamma(x,0)dx = \frac{A_2 q_{w1}}{L}\int_0^{\mu L} dx + \frac{\ln[S_2+1]}{L}\int_{\mu L}^{L} dx = \mu A_2 q_{w1} + (1-\mu)\ln[S_2+1] \quad (8)$$

$\bar{\Gamma}$ can be either positive or negative. In the latter case a complete evaporation of droplets in the course of mixing takes place.

The solution of Eq. (6) with the initial condition (7) is (Polyanin et al., 2004):

$$\Gamma(x,t) = \sum_{n=0}^{\infty} a_n \exp\left(-\frac{Kn^2\pi^2 t}{L^2}\right)\cos\left(\frac{n\pi x}{L}\right) = \mu A_2 q_{w1} + (1-\mu)\ln[S_2+1] - 2\left(\ln[S_2+1] - A_2 q_{w1}\right)\sum_{n=1}^{\infty}\frac{\sin(n\pi\mu)}{n\pi}\exp\left(-\frac{Kn^2\pi^2 t}{L^2}\right)\cos\left(\frac{n\pi x}{L}\right) \quad (9)$$

One can see that function $\Gamma(x,t)$ depends on three independent parameters $A_2 q_{w1}$, S_2 and μ. This function does not depend on the shape of the initial DSD in the cloud volume. In the final state when $t \to \infty$, $\Gamma(x,t)$ is :

$$\Gamma(t=\infty) = \mu A_2 q_{w1} + (1-\mu)\ln[S_2+1] \quad (10)$$

Therefore, $\Gamma(t=\infty)$ depends on the cloud fraction and the initial values of liquid water mixing ratio in the cloud volume and the relative humidity in initially dry volume.

The final equilibrium values of supersaturation $S(x,\infty)$ and liquid water mixing ratio $q_w(x,\infty)$ can be calculated using Eq. (5). The case $\Gamma(t=\infty)>0$ corresponds to the equilibrium state with $S(x,\infty)=0$ and $q_w(x,\infty) = \mu q_{w1} + (1-\mu)\dfrac{\ln[S_2+1]}{A_2}$, when droplets remain, but do not evaporate any longer.

The case $\Gamma(t=\infty)<0$ corresponds to the equilibrium state with $q_w(x,\infty)=0$ and $S(x,\infty)=(1+S_2)^{1-\mu}\exp\left(\mu A_2 q_{w1}\right)-1$. In this equilibrium state droplets are totally evaporated, and volume remains subsaturated $S(x,\infty)<0$. At given q_{w1} and S_2, there is a critical value of the cloud fraction μ_{cr} which separates these two possible final equilibrium states. This critical value corresponds to $\Gamma(t=\infty)=0$ and can be calculated from Eq. (10) as:

$$\mu_{cr}=\frac{\ln\left[S_2+1\right]}{\ln\left[S_2+1\right]-A_2 q_{w1}} \qquad (11)$$

Another expression for μ_{cr} was formulated in Pt1.

The examples of spatial-temporal variations of function $\Gamma(x,t)$ for different cloud fractions and initial RH=80% are shown in **Figure 2.**

Fig 2 here

Upper panels $\mu=0.1$ correspond to the case of final total droplet evaporation and negative final function Γ, whereas the middle and bottom rows $\mu=0.5$ and $\mu=0.9$ illustrate partial evaporation cases when the total mixing volume reaches saturation. It is interesting that the time required for the final equilibrium state to be reached practically does not depend on the cloud fraction, being ~180 seconds for the illustrated cases. The cases $\mu=0.1$ and $\mu=0.9$ demonstrate a strong non-symmetric spatial variability of $\Gamma(x)$ function during the first 50 seconds. At $\mu=0.5$, a nearly full compensation between saturation deficit in the dry volume and available liquid water in the cloud volume takes place if at the equilibrium state $S(x,\infty)=q_w(x,\infty)=\Gamma(x,\infty)=0$. However, the compensation at $\mu=0.5$ is not full because of the nonlinearity of Γ in Eq. (5).

Diffusion-evaporation equation for DSD

To formulate the diffusion-evaporation equation we use a simplified equation for droplet evaporation (Pruppacher and Klett, 1997), in which the curvature term and the chemical composition term are omitted

$$\frac{d\sigma}{dt} = \frac{2S}{F} \tag{12}$$

where $F = \frac{\rho_w L_w^2}{k_a R_v T^2} + \frac{\rho_w R_v T}{e_w(T) D} = const$ (Notations of other variables are presented in Appendix.)

The solution of Eq. (12) is

$$\sigma(t) = \frac{2}{F}\int_0^t S(t')dt' + \sigma_0 \tag{13}$$

Eq. (13) means that in the course of evaporation, distribution $g(\sigma)$ shifts to the left without changing its shape. The diffusion-evaporation equation for function $g(x,t,\sigma)$ can be written in the form

$$\frac{\partial g}{\partial t} = K\frac{\partial^2 g}{\partial x^2} + \frac{\partial}{\partial \sigma}\left(\frac{d\sigma}{dt} g\right) \tag{14}$$

Combining Eqs. (12) and (14) yields

$$\frac{\partial g(x,t,\sigma)}{\partial t} = K\frac{\partial^2 g(x,t,\sigma)}{\partial x^2} + \frac{2S}{F}\frac{\partial g(x,t,\sigma)}{\partial \sigma} \tag{15}$$

Eq. (15) is similar to the diffusion-evaporation equation for size distribution function used in Pt 3. The first term on the right hand side of Eq. (15) describes the effect of turbulent diffusion, while the second term describes the changes of size distribution due to droplet evaporation. To close this equation, one can use Eq. (5) written as

$$S(x,t) = \exp\left[\Gamma(x,t) - A_2 q_w(x,t)\right] - 1, \quad (16)$$

and the equation for liquid water mixing ratio

$$q_w(x,t) = \frac{4\pi\rho_w}{3\rho_a}\int_0^\infty \sigma^{3/2} g(x,t,\sigma)d\sigma \quad (17)$$

The equation system (15-17) for distribution $g(x,t,\sigma)$ should be solved under the following initial condition

$$g(x,0,\sigma) = \begin{cases} g_1(\sigma) & \text{if} \quad 0 \le x < \mu L \\ 0 & \text{if} \quad \mu L \le x < L \end{cases} \quad (18)$$

and using the Neumann boundary conditions

$$\frac{\partial g(0,t,\sigma)}{\partial x} = \frac{\partial g(L,t,\sigma)}{\partial x} = 0 \quad (19)$$

These equations were solved numerically on a linear grid of droplet radii r_j being within the range 0-50 μm, where $j = 1...50$ are the bin numbers. The number of grid points along the x-axis was set equal to 81. In numerical calculations, the "evaporation term" in Eq. (15) was approximated as

$$\frac{2S}{F}\frac{\partial g(x,t,\sigma)}{\partial \sigma} \approx \frac{g\left(x,t,\sigma + \frac{2S}{F}\Delta t\right) - g\left(x,t,\sigma\right)}{\Delta t}. \quad (20)$$

A shift and subsequent remapping of DSD using the method proposed by Kovetz and Olund's (1969) were implemented to solve Eq. (20) with the help of MATLAB solver PDEPE. After calculation of $g\left(x,t,\sigma_j\right)$ function, DSD $f(x,t,r_j)$ was calculated using the relationship $f(x,t,r_j) = 2r_j g(x,t,\sigma_j)$.

305

306 **3. Spatial-temporal variations of DSD and of DSD parameters**

307 Mixing may take a significant time. Cloud microphysical parameters measured in *in-situ*
308 observations correspond to different stages of this transient mixing process. During mixing,
309 DSDs and its parameters change substantially, which makes it reasonable to analyze these
310 time changes.

311 **Figure 3** shows time evolution of initially narrow DSD in the centers of the cloudy volume
312 and of the initially dry volume. The values of DSD in the initially cloudy volume decrease
313 while there are no significant changes in the DSD shape. At $\mu = 0.7$, the modal droplet
314 radius remains unchanged during mixing staying equal to 10 μm . At $\mu = 0.3$ the effect of
315 droplet diffusion on DSD is stronger, and mixing leads not only to a decrease in the DSD
316 values, but also to a decrease in the modal droplet radius in the cloudy volume. At both
317 $\mu = 0.3$ and $\mu = 0.7$, mixing leads to broadening of the initial DSD due to the appearance of
318 the tail of small droplets. The tail of small droplets is especially pronounced in the initially dry
319 volume due to maximum evaporation of penetrated droplets.

320 The rate of the DSD growth in the initially dry volume, depends on the value of the cloud
321 fraction. At a low cloud fraction, the droplet concentration and droplet mass remain
322 substantially lower for the main period of mixing process than that in the cloudy volume. At
323 the same time, the modal DSD radius increases reaching 80% of its maximum value already
324 within the first 5 s. This is due to the fast increase in the relative humidity during mixing, so
325 large droplets penetrating the initially dry volume do not decrease in size anyhow significantly
326 determining the values of modal, mean volume and effective radii. Thus, we see two stages of
327 DSD evolution within the initially dry volumes: at the first stage penetrated droplets evaporate
328 totally or partially forming the tail of small droplets. The formation of the tail of smallest
329 droplets does not lead to a significant changes of the size of the largest droplets. Note that
330 according to equation of diffusion growth/evaporation in of sub-saturation conditions, the rate

of droplet radii decreases inverse proportionally to the droplet radius. It means that if, say, radius of a 2 μm droplet decreases twice during a certain time instance, the radius of 20 μm droplet will decrease by less than 0.1 μm, i.e. remains approximately unchanged. At this stage diffusion of water vapor from cloudy volume and evaporation of penetrating droplets lead to a rapid growth of relative humidity RH. This growth of RH decreases evaporation rate of droplets penetrating initially dry volume later. At the second stage mixing leads to the increase in the droplet number due to droplet diffusion from cloudy volume. Since, RH is high, this diffusion is not accompanied by significant change droplet sizes, so DSD grows similarly at all radii.

Figure 3 here

At the initially wide DSD (**Figure 4**), the modal radii of the DSD do not change. It means that at the initial RH= 80%, mixing and evaporation lead to a fast saturation of the initially dry volume, after which the peak radius remains unchanged in this volume. In the initially cloud volume RH remains close to 100% so the DSD decrease is related to dilution by initially dry air.

Figure 4 here

It is interesting that at $\mu = 0.3$, the maximum value of the DSD maximum in the initially dry volume is reached during the transition period (Fig.4, at t=80s), and then decreases toward the equilibrium state. This behavior is caused by the competition between the diffusion and droplet evaporation.

Figure 5 shows spatial dependences of droplet concentration, LWC and the mean volume radius within the mixing volume at different time instances at narrow initial DSD. At small

values of the cloud fraction, diffusion of water vapor and droplets, as well as droplet evaporation lead to a fast decrease in droplet concentration and in LWC in the initially cloud volume. The mean volume radius in this volume decreases by about 15% in the course of mixing. It is natural that at large cloud fraction, droplet concentration and LWC in the initially cloudy volume decrease slowly, while these quantities in the initially dry volume increase rapidly. At both small and large cloud fractions, the mean volume radius in the initially dry volume grows rapidly during the mixing toward its values in the initially cloudy volumes, even if droplet concentration and LWC remain much lower than in the adjacent cloud volume.

Figure 5 here

Figure 6 shows the spatial dependences of droplet concentration, LWC and the mean volume radius within the mixing volume at different time instances at wide initial DSD.

Figure 6 here

A specific feature of mixing at a wide DSD is the increase in the mean volume radius, so the ratio $\frac{r_v}{r_{v0}} > 1$. In the course of mixing, the mean volume radius maximum is reached in the initially dry volumes. This result can be attributed to the fact that in this volume smaller droplets fully evaporate, so the concentration of large droplets increases with respect to concentration of smaller droplets (Fig. 4, right column). Scattering diagrams plotted using *in-situ* observations often contain points or groups of points with $\frac{r_v}{r_{v0}} > 1$ (or $\frac{r_e}{r_{e0}} > 1$, where r_e is effective radius) within wide range of normalized droplet concentration (e.g., Burnet and

382 Brenguier, 2007; Krueger et al., 2006, Gerber et al., 2008). The result obtained in the present
383 study shows that the behavior of $\frac{r_v}{r_{v0}}$ with time in the course of mixing may depend of the
384 DSD shape in the initially cloud volume that determines relationship between concentrations
385 of small and large droplets in course of mixing. Of course, the DSD shape is only one possible
386 reason of appearance of points with $\frac{r_v}{r_{v0}} > 1$ on the scattering diagram.

387 We see that the transition to the final equilibrium state within the volume with the spatial
388 scale of 40 m is about 5 min (Fig. 8), which is a comparatively long period of time compared
389 to the characteristic times of other microphysical processes, including droplet evaporation.
390 During this time the DSD changes substantially, especially at small cloud fraction. The mean
391 volume radius in the initially dry volume increases much faster than LWC. As a result, mean
392 volume radius in such volume rapidly reaches the values typical of cloudy air, while LWC
393 still remains substantially lower than in the cloudy volume. Despite some DSD broadening,
394 the final DSDs in the mixing volume resemble those in the initially cloud volumes. The main
395 effect of mixing is lowering the DSD values as the cloud fraction decreases.
396

397 **4. Equilibrium state and mixing diagram**

398 This study reconsiders the classical theory of mixing diagrams. In the classical theory
399 two volumes (cloudy and droplet free) mix with each other within a given unmovable mixing
400 volume (see review by Korolev et al., 2016). Mixing diagrams are typically plotted for times
401 when all variables become uniform within the mixing volume, i.e when the equilibrium state
402 is reached. We plot the mixing diagram using the same simplifications used in the plotting
403 classical mixing diagrams, namely: no vertical motions and no collisions are assumed. These
404 assumptions allow to reveal better the microphysical effects of turbulent mixing. It is widely
405 assumed that the mixing type is determined by the Damkohler number that depends only on
406 drop relaxation time and mixing time. No averaged vertical velocity and no collision rate are

included into this criterion.

We extend the theory, however, in several important aspects concerning microphysical effects: a) we consider time dependent process of mixing and b) initial droplet size distributions are assumed polydisperse.

Mixing considered in the present study always leads to the equilibrium state. As was explained above, two equilibrium states are possible. The first one is characterized by the total evaporation of cloud droplets $q_w(x,\infty)=0$, whereas the second one occurs if the air in the mixing volume becomes saturated, i.e. when $S(x,\infty)=0$. At the given initial values of q_{w1} in the cloud volume and of S_2 in the initially dry volume, there always exists the cloud fraction μ_{cr} (Eq. 11) separating these two states.

4.1. The process of achieving the equilibrium state

Figure 7 shows the dependences of the time required to reach the equilibrium on the cloud fraction, at different initial relative humidity values in the dry volume and two initial DSDs (the parameters are presented in Tab.1). The characteristic time is defined here as the time from the beginning of mixing to the time instance when inequality $\delta=\dfrac{\bar{N}(t)-\bar{N}(\infty)}{\bar{N}(0)-\bar{N}(\infty)}<0.01$ becomes valid. The mean droplet concentration is calculated by averaging along x-axes ($\bar{N}(t)=\dfrac{1}{L}\int_0^L N(x,t)dx$). In case of a total evaporation, $\bar{N}(\infty)=0$.

Figure 7 here

Each curve in Fig. 7 consists of two branches. The left branches correspond to the total evaporation regime, while the right branches correspond to the partial evaporation at equilibrium. The maximum time corresponds to the situation when the available amount of

liquid water is approximately equal to the saturation deficit. A similar result was obtained in Pt1 and Pt2 for homogeneous mixing. The maximum values of the characteristic time are about 4 min for a mixing volume of 40 m in length. The right branches show that the characteristic time decreases with increasing cloud fraction. Despite some differences in the curve slopes, the characteristic times for wide and narrow DSD are quite similar.

Figure 8 shows dependences of normalized cube of the mean volume radius on the cloud fraction at different time instances for two values of x: $x = 0$ (solid lines) corresponds to the initially cloudy volume, and $x = L$ (dashed line) corresponds to the initially dry volume. The figure is plotted for the narrow DSD for two values of RH_2: 60% and 95%. Despite the fact that the diffusion-evaporation equation allows simulating using any initial RH, we do not consider in our examples the cases of very low RH of dry volume. It is because at very low RH, say, RH=20%, the cloud fraction should exceed 0.8 to prevent total droplet evaporation in the equilibrium state (at LWC=1 g/kg). At the same time, we are interested in the equilibrium state at which droplets exist. Note that at the lateral edges of warm Cu a shell of humid air arises around cloud, so RH of the entrained air should be high enough (e.g. Gerber et al., 2008).

Figure 8 here

The curve plotted for the time instance of 300 s corresponds to the equilibrium state (hereafter the equilibrium curve). The curves above the equilibrium curve correspond to the initially cloudy volume, and the curves below the equilibrium curve correspond to the initially dry volume. One can see how curves of both types approach the same final state. During the mixing the curves move over the $\left(\frac{r_v}{r_{v0}}\right)^3 - \mu$ plane toward the equilibrium curve. As a result,

455 the curves plotted in Fig.8, corresponding to different time instances of the mixing, together
456 cover the entire area of the panels.

457 During this movement the distance from the curves to the horizontal line $\left(\frac{r_v}{r_{v0}}\right)^3 = 1$ changes,
458 and the curves slopes increase. In our case of $L = 40\,\text{m}$, the mixing remains inhomogeneous
459 the during entire mixing process, so the change in the distance from the curves to the
460 horizontal line $\left(\frac{r_v}{r_{v0}}\right)^3 = 1$ characterizes the temporal changes over the mixing process, but not
461 a change in mixing type.

462 It is noteworthy in this relation that scattering diagrams plotted using *in-situ* observations
463 reflect mixing between different multiple volumes at different stages of the mixing process.
464 Accordingly, points in the scattering diagrams can be far from the equilibrium location. Fig. 8
465 indicates, therefore, that scattering diagrams show snapshots of transient mixing process when
466 the distance from points in the diagrams to line $\left(\frac{r_v}{r_{v0}}\right)^3 = 1$ characterize the stage of the
467 mixing process, but not the mixing type.

468 The dependences of normalized cube of the mean volume radius on the cloud fraction at
469 different time instances at wide DSD also indicate approaching to the equilibrium curve,
470 while all the curves correspond to $\left(\frac{r_v}{r_{v0}}\right)^3 > 1$ (not shown).

471 Note that in several studies normalized effective radius is used for plotting scattering and
472 mixing diagrams, but not mean volume radius (Gerber et al. 2008; Freud et al., 2011).
473 Comparison of scattering and mixing diagrams in the study plotted using mean volume and
474 effective radii did not reveal any significant differences (not shown).

475

476 **4.2. Mixing diagrams**

Using the diffusion-evaporation equations (15-17) we calculated the equilibrium DSD for different initial relative humidity values and different cloud fractions. Each calculation was performed for both narrow and wide initial DSD (parameters shown in Tab.1). These equilibrium DSD were used to calculate mixing diagrams showing dependences of normalized cube of the effective radius on the cloud fraction.

The corresponding mixing diagrams for homogeneous mixing case were also calculated for comparison. To this effect, the supersaturation and DSD in both the cloud and the dry volumes were aligned, taking into account the cloud fraction value μ. The alignment led to the following initial values of supersaturation and DSD within the mixing volume:

$$S_0 = (1-\mu)S_2; \quad g_0(\sigma) = \mu g_1(\sigma) \tag{21}$$

Upon the alignment, time evolution values of DSD under homogeneous evaporation in an adiabatic immovable parcel were calculated until the equilibrium state was reached. These equilibrium DSD were used to calculate mixing diagrams for homogeneous mixing. To do this, we used the parcel model proposed by Korolev (1995) that describes evaporation by means of equations with temperature-dependent parameters. **Figure 9** shows the mixing diagrams plotted for initial narrow and wide DSD cases.

Figure 9 here

While all the curves in the mixing diagram for narrow DSD are below the straight line $\left(\frac{r_v}{r_{v0}}\right)^3 = 1$, the curves for wide DSD are above this line. The explanation of this effect is given in Section 3 (Fig. 6). The curves plotted for homogeneous and inhomogeneous mixing

demonstrate an important feature. Namely, at given values of RH and q_{w1} in the initially dry volume, the values μ_{cr} of the cloud fraction at which all the droplets evaporate are approximately the same for any type of mixing. This condition is the consequence of the mass conservation law determined by Eq. (11) and does not depend of the initial DSD shape. In standard mixing diagrams (e.g. Lehmann et al., 2009; Gerber et al., 2008; Freud et al., 2011), the horizontal straight line $\left(\frac{r_v}{r_{v0}}\right)^3 = 1$ (or $\left(\frac{r_e}{r_{e0}}\right)^3 = 1$) is typically plotted for the entire range of the cloud fraction [0...1], while the curves corresponding to homogeneous mixing are plotted for different RH within the range $[\mu_{cr}(RH_2)...1]$. As a result, the high difference between extremely inhomogeneous and homogeneous mixing types is clearly seen at low RH and at small cloud fractions. The condition that μ_{cr} is the same for different mixing types indicates that the mixing diagrams may look nearly similar for $\mu > \mu_{cr}$. It means that the range of the cloud fractions required for comparison of diagrams aimed at determination of a mixing type shortens as RH_2 values in the surrounding air decrease.

The comparison of the left and the right panels in Fig. 9 shows that the differences between the diagrams for homogeneous and inhomogeneous mixing types are more pronounced for initially narrow DSD. The maximum difference should take place for monodisperse DSD considered in in Pt1, Pt2 and Pt3. Within the range of $\mu > \mu_{cr}$, the distance between the curves corresponding to different mixing regimes is small even for narrow DSD and low RH_2. The lower difference is related to the fact that at high RH_2 the curves in the mixing diagrams are close to the horizontal straight line in both regimes, while at low RH_2, μ_{cr} is small and both curves should drop to zero in the vicinity of $\mu = \mu_{cr}$.

As regards the wide DSD case, the difference between the curves corresponding to different mixing type is negligible (Fig. 9, right)

526 **4.3. Effect of the relative humidity**

527 In measurements carried out at cloud boundaries and in cloud simulations, the cloud
528 fraction is not known, therefore it is widely accepted to use normalized droplet concentration
529 instead of the cloud fraction (Burnet and Brenguier, 2007; Gerber et al., 2008: Lehmann et al.,
530 2009). Droplet concentration is normalized by the maximum value along the airplane traverse.
531 The difference between the cloud fraction and normalized droplet concentration is obvious:
532 the cloud fraction is a parameter given as the initial condition. At the same time, normalized
533 droplet concentration changes with time and space due to complete evaporation of some
534 droplet fraction. **Figure 10** shows dependencies of normalized droplet concentration on the
535 cloud fraction at the equilibrium final state of mixing. One can see a substantial deviation
536 from 1:1 linear dependence, especially at low RH. As we know, droplet concentration
537 decreases in the course of both homogeneous and inhomogeneous mixing if the initial DSD
538 are polydisperse. The fraction of totally evaporating droplets increases with decreasing RH_2.
539 As expected, droplet concentration in homogeneous mixing is higher than that in
540 inhomogeneous mixing. The difference between droplet concentrations at wide DSD is lower
541 than at narrow DSD.

542

543 **Fig. 10 here**

544

545 **Figure 11** shows the dependencies $\left(\frac{r_v}{r_{v0}}\right)^3$ on normalized droplet concentration for narrow
546 and wide DSD in inhomogeneous mixing. The normalization by droplet concentration in the
547 initially cloud volume at $t = 0$ was used. Taking into account the dependences of normalized
548 droplet concentration on the cloud fraction μ (Fig. 10), one can get the curves shown in Fig.
549 11 which actually coincide at different RH_2. The lack of the sensitivity to RH_2 can be
550 attributed to the fact that a decrease in RH leads to a decrease in normalized droplet

551 concentration, so the curves corresponding to low RH in Fig. 9 shift to the left when the
552 normalized droplet concentration is used instead of μ. The shape of the dependences in Fig
553 11 (right) is explained by an increase in the mean volume radius with decreasing droplet
554 concentration.

555

556 **Fig 11 here**

557

558 Thus, the mixing diagrams plotted in the plane $\left(\frac{r_v}{r_{v0}}\right)^3$ vs normalized droplet
559 concentration do not depend on the relative humidity of the surrounding dry air. This result
560 indicates an additional difficulty in distinguishing between mixing types based on scattering
561 diagrams plotted using *in-situ* data in these axes. The concentration of observed points in
562 these scattering diagrams close to the line $\left(\frac{r_v}{r_{v0}}\right)^3 = 1$ is often interpreted as an indication of
563 homogeneous mixing, but at high RH in the surrounding air (Gerber et al., 2008; Lehmann et
564 al., 2009). High values of RH in the penetrating air volumes are usually explained by
565 formation of a layer of most air around the cloud boundary (Gerber et al., 2008, Knight and
566 Miller, 1998).

567 The reference values of droplet concentration and the effective radius used for
568 normalization in the present study are taken as the initial values in the cloud volume before it
569 mixes with the neighbouring dry volume. In real *in-situ* measurements the reference values of
570 these quantities are typically chosen in a less diluted cloud volume along the airplane traverse.
571 This reference volume may be quite remote from the particular mixing volume. It can lead to
572 a shift of the mixing diagram with respect to the $\left(\frac{r_v}{r_{v0}}\right)^3 = 1$ line, as well as to a large variation

573 in mixing diagram shapes, unrelated, however, to the mixing type (e.g., Lehmann et al.,
574 2009).
575
576 **5. Discussion and conclusion**
577 This study extends the analysis of mixing performed in Pt3 where the diffusion-
578 evaporation equation served as the basis, the initial DSD were assumed monodisperse and
579 the cloud fraction was chosen as $\mu = 1/2$. In the present study, the analysis focuses on the
580 temporal and spatial evolution of initially polidisperse DSD and investigates mixing diagrams
581 obtained for narrow and wide initial DSD within a wide range of the cloud fraction values (0.1
582 - 0.95). It is shown that results of mixing and the structure of mixing diagrams depend on the
583 initial DSD shape. This finding indicates that mixing is a multi-parametrical problem that
584 cannot be determined by a single parameter (e.g. the Damkölher number as often assumed) or
585 even by two parameters (the Damkölher number and the potential evaporation parameters as
586 assumed in Pt3). The temporal changes of DSD and their moments during mixing are
587 calculated. Although DSD broaden, they tend to remain similar to the original DSD. The main
588 changes come from the cloud air dilution by the dry air, which leads to a decrease in droplet
589 concentration for all droplet sizes. The changes of DSD and its shape are minimum in the
590 initially cloud volumes, especially at significant cloud fractions. The droplet radii
591 corresponding to the DSD peak do not change anyhow significantly. In the initially dry
592 volumes, mixing and evaporation of penetrated droplets leads to a rapid increase in RH.
593 Consequently, large droplets penetrating these volumes do not change their sizes significantly.
594 As a result, the mean volume radius in these volumes rapidly increases and reaches the values
595 typical of cloud volumes, while LWC remains lower than in the cloud volume for most of the
596 mixing time. At narrow DSD, the mean volume (and effective) radius remains smaller than
597 that in the initially cloud volume. At wide DSD, the mean volume (and effective) radius may
598 become larger than that in the initial DSD. This increase in the effective radius is attributed to

599 the fact that evaporation of smaller droplets leads to the increase in the fraction of larger
600 droplets in the DSD. In this study, and in Pt3 it is shown that mixing leads to DSD
601 broadening. This contrasts with the classical theory, when initially monodisperse DSDs
602 remain monodisperse in course of mixing. This problem is analyzed in detail in Pt 3. Note
603 that in real clouds DSD there are many mechanism leading to DSDs broadening (e.g. Pinsky
604 and Khain 2002).

605 Dependences of normalized cube of the mean volume radius on the cloud fraction
606 $\left(r_v / r_{v0}\right)^3$ as a function of μ at different time instances form the set of curves filling the entire
607 $\left(r_v / r_{v0}\right)^3 - \mu$ plane. Therefore, both the slope and the distance of these curves in respect to
608 the horizontal line $\left(r_v / r_{v0}\right)^3 = 1$ change with time. It means that this distance characterizes
609 the temporal changes in the course of mixing, but not the mixing type (which remains
610 inhomogeneous during the entire mixing time). The mixing process is comparatively long
611 (several minutes), so the final equilibrium stage is hardly achievable in real clouds.

612 It is highly significant that the critical values of the cloud fraction μ_{cr} corresponding to
613 total droplet evaporation are the same for any mixing type. It means that the curves in a
614 mixing diagram corresponding to homogeneous and inhomogeneous mixing types should be
615 compared only within the range of $\mu > \mu_{cr}$. The range width of $\mu > \mu_{cr}$ decreases with
616 decreasing relative humidity in the initially dry volume. Taking into account significant
617 scattering of observed points, this condition greatly hampers the problem of how to
618 distinguish between mixing types,

619 Another important result of the study is that mixing diagrams for homogeneous and
620 inhomogeneous mixing plotted for polydisperse DSD do not differ much. The largest
621 difference takes place for initially narrow DSD (the maximum difference takes place for
622 initially monodisperse DSD), but even in this case the difference is not large enough to
623 reliably distinguish mixing type, owing the significant scatter of observed data. At wide DSD,

this difference between mixing diagrams for homogeneous and inhomogeneous becomes negligibly small.

The cloud fraction μ is a predefined parameter and is not determined from observations. Consequently, in the analysis of *in-situ* measurements the normalized droplet concentration is typically used instead of the cloud fraction. However, there is a significant difference between the cloud fraction prescribed a priori and the normalized droplet concentration that changes due to total evaporation of some fraction of droplets. We have shown that the utilization of normalized droplet concentration in mixing diagrams is not equivalent to the utilization of the cloud fraction. The important conclusion is that when mixing diagrams are plotted using the normalized concentration, the sensitivity to RH disappears. This conclusion is valid even when RH in the initially dry volume is as low as 60%. This conclusion clearly contradicts the wide-spread assumption that mixing types can be easily distinguished in mixing diagrams in case of low relative humidity of the surrounding air.

In the present study as well as in Pt3 and modeling studies performed by Andrejczuk et al. (2006, 2009), Khain et al. (2017) it is shown that time needed to establishing of equilibrium either quite long or even never reached. It means that the scattering diagrams observed in situ are just snapshots of the transient mixing process. In order to show how different are the equilibrium and intermediate states we investigate the transition to such equilibrium assuming that the mixing volume remains adiabatic (i.e. isolated) during the entire period of mixing. This is, of course, a serious simplification made to compare the results with those predicted by classical concept. Another simplification of the model is the neglecting the intermittency in the process of mixing that takes place in real clouds.

To sum up, our general conclusion is that the simplifications underlying the classical concept of mixing are too crude, making it impossible to use scattering diagrams for comprehensive analysis of mixing and especially for determination of mixing types. At the

same time, scattering diagrams may contain useful information concerning intensity of mixing, the DSD width and other parameters of DSDs (see Khain et al., 2017).

Acknowledgements

This research was supported by the Israel Science Foundation (grants 1393/14, 2027/17) and the Office of Science (BER) of the US Department of Energy (Award DE-SC0006788, DE-FOA-0001638). Codes of the diffusional-evaporation model are available upon request.

.

Appendix. List of symbols

Symbol	Description	Units
A_2	$\frac{1}{q_v}+\frac{L_w^2}{c_p R_v T^2}$, coefficient	-
a_n	Fourier series coefficients	-
C	Richardson's law constant	-
c_p	specific heat capacity of moist air at constant pressure	J $kg^{-1}K^{-1}$
D	coefficient of water vapor diffusion in air	m^2 s^{-1}
Da	*Damkölher* number	-
e	water vapor pressure	N m^{-2}
e_w	saturation vapor pressure above flat surface of water	N m^{-2}
F	$\left(\frac{\rho_w L_w^2}{k_a R_v T^2}+\frac{\rho_w R_v T}{e_w(T) D}\right)$, coefficient	m^{-2} s
$f(r)$	droplet size distribution	m^{-4}
$g(r)$	droplet size distribution	m^{-5}

$g_0(\sigma)$	initial distribution of square radius in homogeneous mixing	m^{-5}
$g_1(\sigma)$	initial distribution of square radius	m^{-5}
k_a	coefficient of air heat conductivity	$J\ m^{-1}s^{-1}K^{-1}$
K	turbulent diffusion coefficient	m^2s^{-1}
L	characteristic spatial scale of mixing	m
L_w	latent heat for liquid water	$J\ kg^{-1}$
N	droplet concentration	m^{-3}
N_0	Parameter of Gamma distribution	m^{-3}
$\bar{N}$	mean droplet concentration	m^{-3}
N_1	initial droplet concentration in cloud volume	m^{-3}
p	pressure of moist air	$N\ m^{-2}$
q_v	water vapor mixing ratio (mass of water vapor per 1 kg of dry air)	-
q_w	liquid water mixing ratio (mass of liquid water per 1 kg of dry air)	-
q_{w1}	liquid water mixing ratio in cloud volume	-
R	$\frac{S_2}{A_2 q_{w1}}$, non-dimensional parameter	-
R_a	specific gas constant of moist air	$J\ kg^{-1}K^{-1}$
R_v	specific gas constant of water vapor	$J\ kg^{-1}K^{-1}$
r	droplet radius	m
r_1	initial droplet radius	m
r_e	effective radius	m
r_{e0}	initial effective radius	m
S	$e/e_w - 1$, supersaturation over water	-
S_2	initial supersaturation in the dry volume	-

S_0	initial supersaturation in homogeneous mixing	-
T	temperature	K
t	time	s
x	distance	m
α	parameter of Gamma distribution	-
β	parameter of Gamma distribution	m^{-1}
Δt	time step	s
μ	cloud fraction	-
μ_{cr}	critical cloud fraction	-
ε	turbulent dissipation rate	$m^2 s^{-3}$
$\Gamma(x,t)$	conservative function	-
ρ_a	air density	kg m^{-3}
ρ_w	liquid water density	kg m^{-3}
σ	square of droplet radius	m^2

661

662

663

664

665

666

667

668

669

670

671

672

673 **References**

674

675 Andrejczuk, M., W. W. Grabowski, S. P. Malinowski, and P. K. Smolarkiewicz, 2006:
676 Numerical simulation of cloud– clear air interfacial mixing: Effects on cloud microphysics. *J.*
677 *Atmos. Sci*., **63**, 3204–3225.

678 Andrejczuk, M., W. W. Grabowski, S. P. Malinowski, and P. K. Smolarkiewicz, 2009:
679 Numerical simulation of cloud–clear air interfacial mixing: Homogeneous versus
680 inhomogeneous mixing, *J. Atmos. Sci.*, **66(8),** 2493-2500, doi:10.1175/2009JAS2956.

681 Bera, S., T. V. Prabha, and W. W. Grabowski, 2016a: Observations of monsoon
682 convective cloud microphysics over India and role of entrainment-mixing, *J. Geophys. Res.*
683 *Atmos*., **121**, 9767–9788, doi:10.1002/2016JD025133.

684 Bera, S., G. Pandithurai and T. V. Prabha, 2016b: Entrainment and droplet spectral
685 characteristics in convective clouds during transition to monsoon. *Atmos. Sci. Let.* **17**, 286–
686 293.

687 Boffetta, G. and Sokolov, I. M., 2002: Relative dispersion in fully developed turbulence:
688 The Richardson's law and intermittency correction, *Phys. Rev. Lett*., **88**, 094501,
689 doi:10.1103/PhysRevLett.88.094501.

690 Burnet, F., and J.-L Brenguier, 2007: Observational study of the entrainment-mixing
691 process in warm convective cloud, *J. Atmos. Sci*., **64**, 1995–2011.

692 Devenish B. J., P. Bartello, J-L. Brenguier, L.R. Collins, W.W. Grabowski, R.H.A.
693 Ijzermans, S.P. Malinovski, M.W. Reeks, J.C. Vassilicos, L-P. Wang, and Z. Warhaft, 2012:
694 Droplet growth in warm turbulent clouds. *Q. J. Roy. Meteorol. Soc.*, **138**, 1401-1429.

695 Freud, E., D. Rosenfeld, and J. R. Kulkarni, 2011: Resolving both entrainment mixing and
696 number of activated CCN in deep convective clouds, *Atmos. Chem. Phys*., **11**, 12,887–12,900,
697 doi:10.5194/acp-11-12887-2011.

698 Gerber H, Frick G, Jensen J.B, and Hudson J.G., 2008: Entrainment, mixing, and
699 microphysics in trade-wind cumulus. *J. Meteorol. Soc. Jpn.*, **86A**. 87-106.
700 Khain, A. P., M. Ovchinnikov, M. Pinsky, A. Pokrovsky, and H. Krugliak, 2000: Notes on
701 the state-of-the-art numerical modeling of cloud microphysics. *Atmos. Res.*, **55**, 159-224.
702 Khain A., Thara V. Prabha, N. Benmoshe, G. Pandithurai, M. Ovchinnikov, 2013: The
703 mechanism of first raindrops formation in deep convective clouds. *J. Geoph. Res.*
704 *Atmospheres*, **118**, 9123–9140.
705 Khain A., M. Pinsky and L. Magaritz-Ronen, 2017: Physical interpretation of mixing
706 diagrams. *J. Geophys. Res.* (in press)
707 Knight C. A. and L. J. Miller, 1998: Early radar echoes from small, warm cumulus: Bragg
708 and hydrometeor scattering. *J. Atmos. Sci.*, **55**, 2974-2992.
709 Korolev, A.V., 1995: The influence of suresaturation fluctuations on droplet size spectra
710 formation. *J. Atmos. Sci.*, **52**, 3620-3634.
711 Korolev A., and I. Mazin, 2003: Supersaturation of water vapor in clouds, *J. Atmos. Sci*.,
712 **60**, 2957-2974.
713 Korolev, A., Khain, A., Pinsky, M., and French, J., 2016: Theoretical study of mixing in
714 liquid clouds – Part 1: Classical concept, *Atmos. Chem. Phys.*, **16**, 9235–9254.
715 Kovetz, A., and B. Olund, 1969: The effect of coalescence and condensation on rain
716 formation in a cloud of finite vertical extent. *J. Atmos. Sci.*, **26,** 1060–1065.
717 Krueger, S. K., Lehr, P. J., & Su, C. W., 2006: How entrainment and mixing scenarios
718 affect droplet spectra in cumulus clouds. In *12th Conference on Cloud Physics, and 12th*
719 *Conference on Atmospheric Radiation,* Madison, WI.
720 Kumar, B., J. Schumacher, and R. A. Shaw, 2014: Lagrangian mixing dynamics at the
721 cloudy–clear air interface. *J. Atmos. Sci*., **71**, 2564-2579.

722 Kumar, B., S. Bera, T. V. Prabha, and W. W. Grabowski, 2017: Cloud-edge mixing:
723 Direct numerical simulation and observations in Indian Monsoon clouds, *J. Adv. Model. Earth*
724 *Syst*., **9**, doi:10.1002/2016MS000731.

725 Lehmann, K.., H. Siebert, and R. A. Shaw, 2009: Homogeneous and inhomogeneous
726 mixing in cumulus clouds: Dependence on local turbulence structure. *J. Atmos. Sci*., **66**, 3641-
727 3659.

728 Magaritz-Ronen. L., M. Pinsky, and A. Khain, 2016: Drizzle formation in stratocumulus
729 clouds: effects of turbulent mixing. *Atmos. Chem. Phys*., **16**, 1849–1862, doi:10.5194/acp-16-
730 1849.

731 Monin, A.S. and Yaglom, A.M. 1975: "Statistical Fluid Mechanics: Mechanics of
732 Turbulence", vol. **2**, MIT Press.

733 Pinsky, M., Khain, A. P., 2002: Effects of in-cloud nucleation and turbulence on droplet
734 spectrum formation in cumulus clouds. *Quart. J. Roy. Met. Soc*., **128**, 1-33.

735 Pinsky, M., Khain, A., Korolev, A., and Magaritz-Ronen, L., 2016a: Theoretical
736 investigation of mixing in warm clouds – Part 2: Homogeneous mixing, *Atmos. Chem. Phys*.,
737 **16**, 9255–9272.

738 Pinsky, M., Khain, A., and Korolev, A., 2016b: Theoretical analysis of mixing in liquid
739 clouds – Part 3: Inhomogeneous mixing, *Atmos. Chem. Phys*., **16**, 9273–9297.

740 Polyanin A. D. and V. F. Zaitsev, 2004: Handbook of nonlinear partial differential
741 equations. Chapman & Hall/CRC, 809 pp.

742 Prabha T. , Khain, A. P., B. N. Goswami, G. Pandithurai, R. S. Maheshkumar, and J. R.
743 Kulkarni, 2011: Microphysics of pre-monsoon and monsoon clouds as seen from in-situ
744 measurements during CAIPEEX. *J. Atmos. Sci.*, **68**, 1882-1901.

745 Pruppacher, H.R., Klett, J.D., 1997. Microphysics of Clouds and Precipitation. 2nd edn.
746 Oxford Press, 914 p.

747 Segal, Y., Khain, A. P., and M. Pinsky, 2003: Theromodynamic factors influencing the
748 bimodal spectra formation in cumulus clouds. *Atmos. Res.* **66**, 43-64.
749 Yang F., R. Shaw, and H. Xue, 2016: Conditions for super-adiabatic droplet growth
750 after entrainment mixing *Atmos. Chem. Phys.*, **16**, 9421–9433, www.atmos-chem-
751 phys.net/16/9421/2016/ doi:10.5194/acp-16-9421-2016.
752 Yum, S. S., J. Wang, Y. Liu, G. Senum, S. Springston, R. McGraw, and J. M. Yeom,
753 2015: Cloud microphysical relationships and their implication on entrainment and mixing
754 mechanism for the stratocumulus clouds measured during the VOCALS project, *J. Geophys.*
755 *Res.*, **120(10)**, 5047-5069, 10.1002/2014JD022802.
756
757
758
759
760
761
762
763
764
765
766
767
768
769
770
771
772

773
774
775
776
777
778
779
780

781 **Tab.1** Parameters of the initial Gamma distributions

DSD	N_0, cm^3	α	β, μm	Modal radius, μm	LWC, g/m^3
Narrow	264.2	101.0	0.1	10.0	1.178
Wide	71.0	4.3	3.1	10.0	1.178

782
783
784
785
786
787
788
789
790
791
792
793
794
795

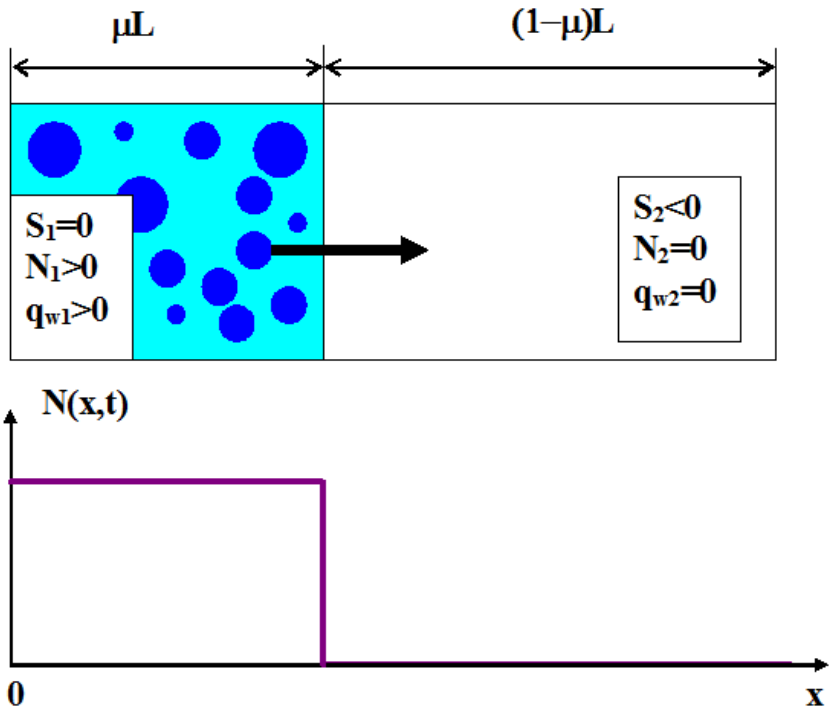

Fig.1. The initial state at $t=0$. The left volume is a saturated cloudy volume; the right volume is an under-saturated dry air volume.

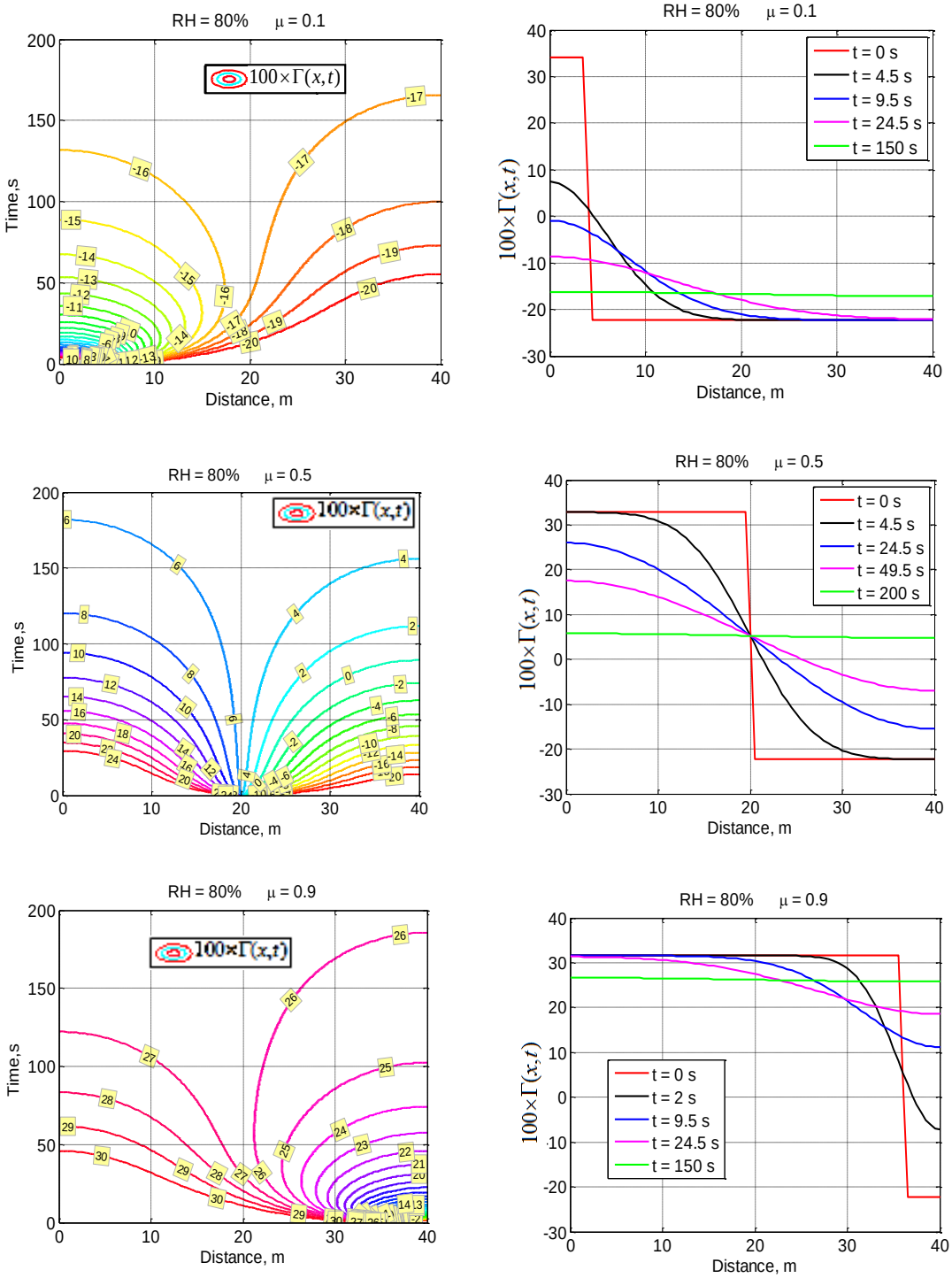

Fig. 2. Spatial-temporal variations of conservative function $100\times\Gamma(x,t)$ for different cloud fractions μ and initial $RH_2 = 80\ \%$.

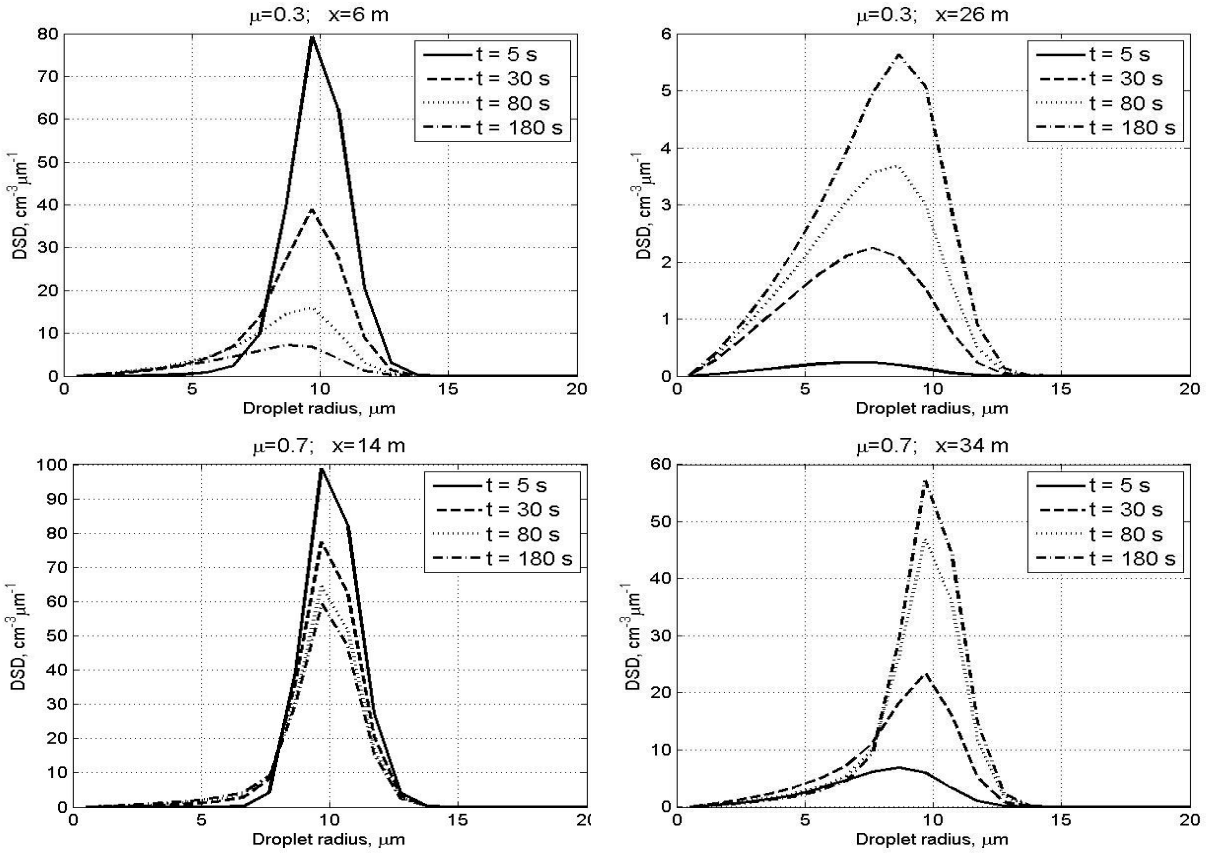

Fig. 3. Time evolution of DSD in the centers of the initially cloudy volume (left) and of the initially dry air volume (right) at initially narrow DSD. The initial mixing parameters are $RH_2 = 80\ \%$, $T = 10^{o}C$, $p = 828.8$ mb and $L = 40$ m.

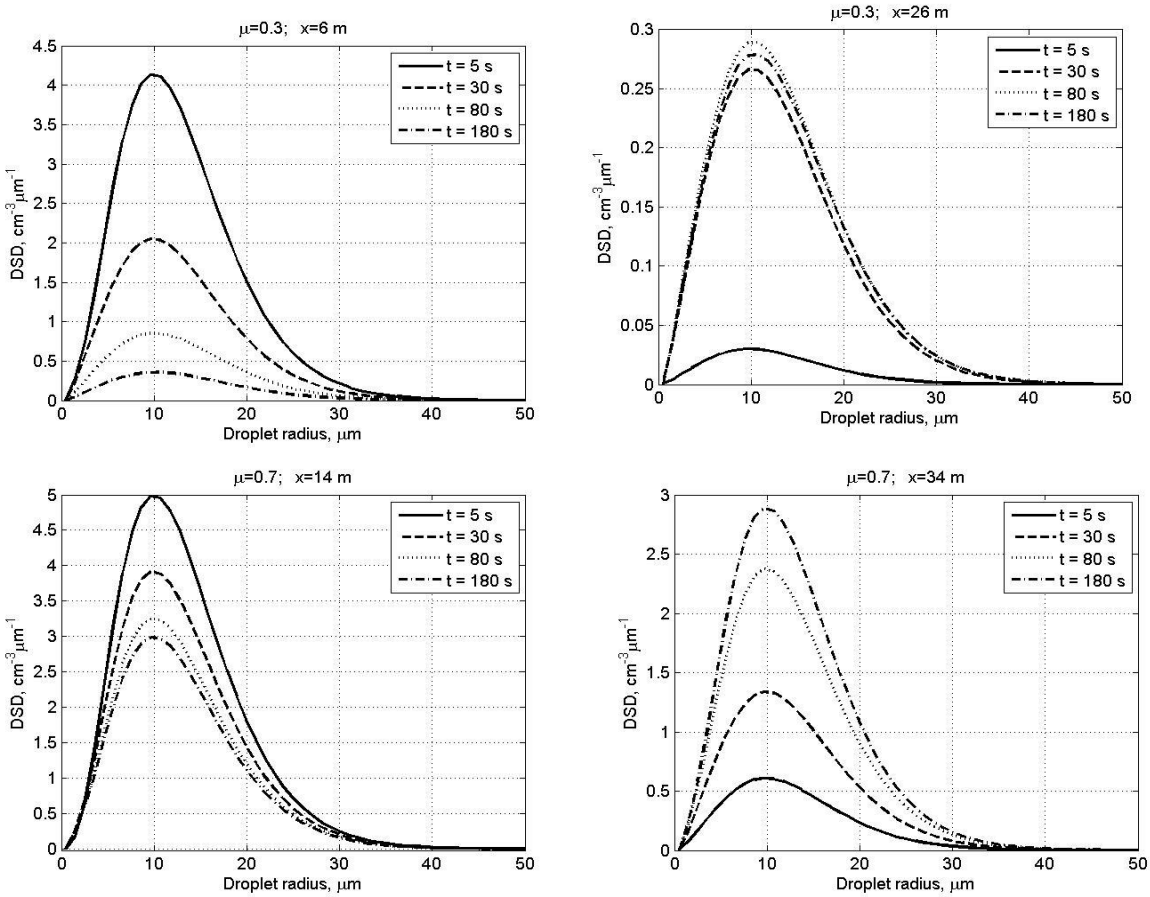

Fig. 4. The same as in Fig. 3, but for the initially wide DSD.

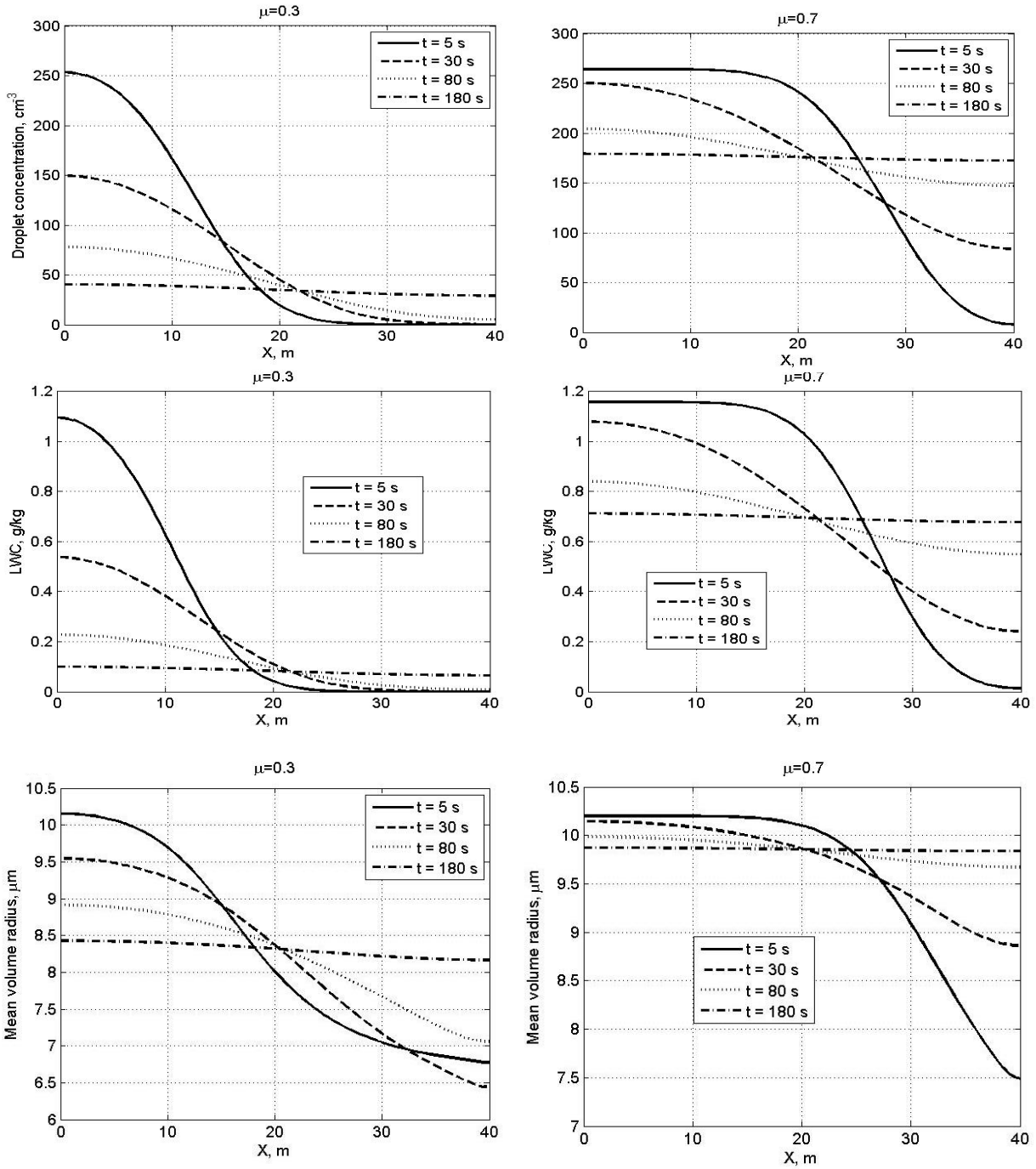

Fig. 5. Spatial dependences of droplet concentration, LWC and the mean volume radius within the mixing volume at different time instances at narrow initial DSD. The initial mixing parameters are $RH_2 = 80\ \%$, $T = 10^{o}C$, $p = 828.8$ mb and $L = 40$ m.

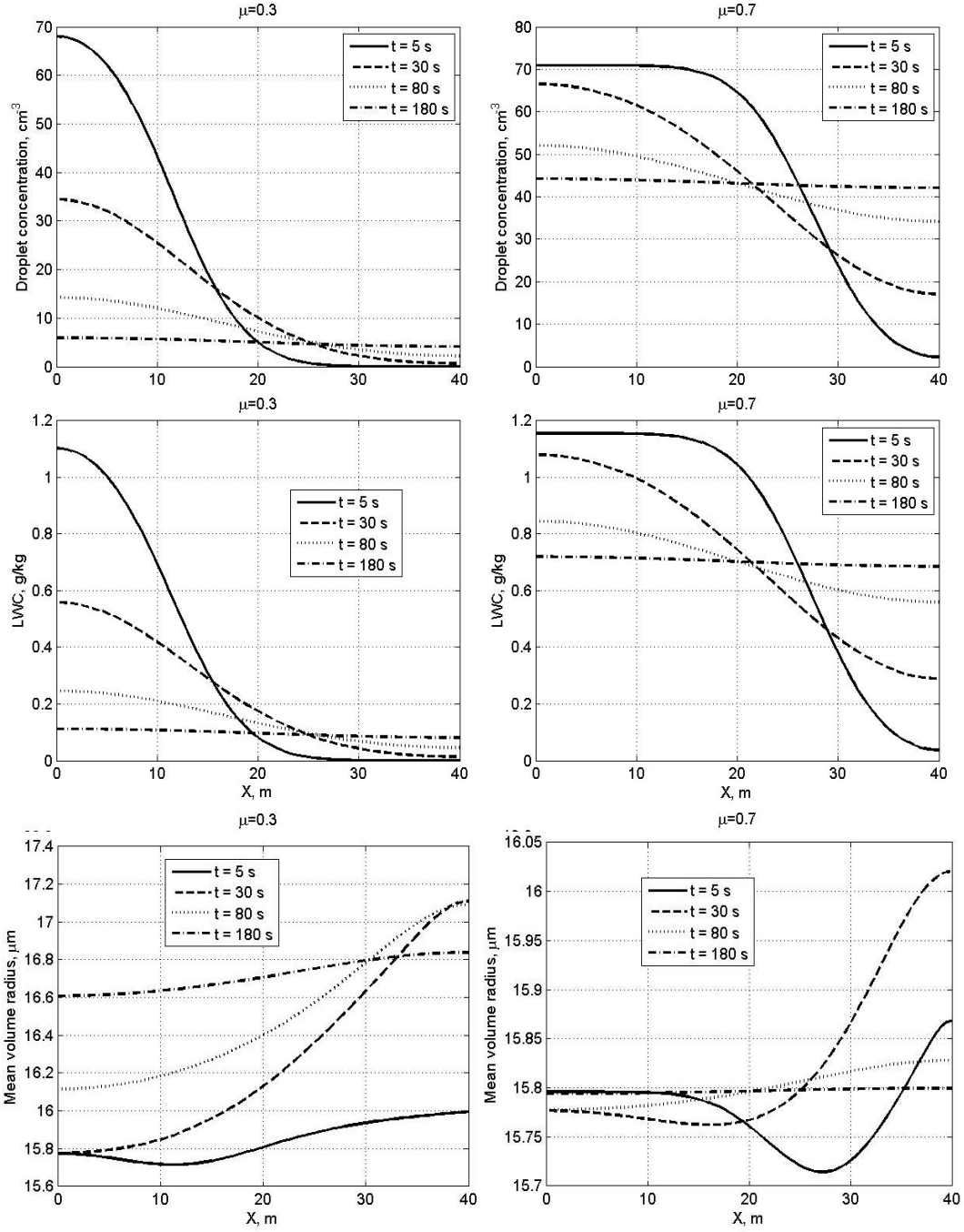

Fig. 6. The same as in Fig. 5, but for wide DSD

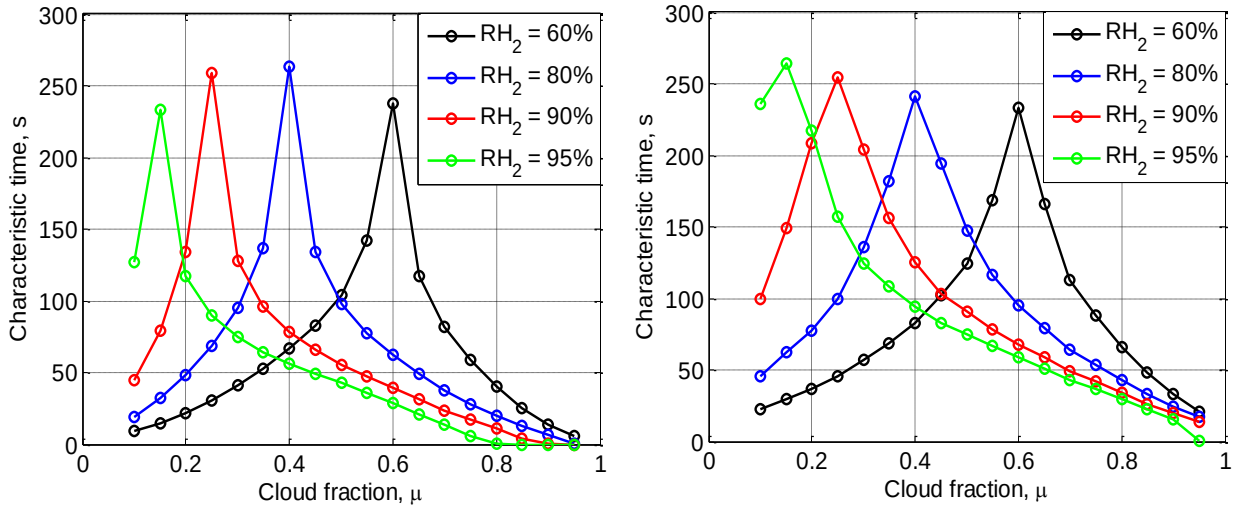

Fig. 7. Time required to reach the equilibrium state vs. the cloud fraction at different initial RH for the initially narrow DSD (left) and the initially wide DSD (right). Parameters of DSD are given in Tab. 1. The initial mixing parameters are $T = 10^{o}C$, $p = 828.8$ mb and $L = 40$ m.

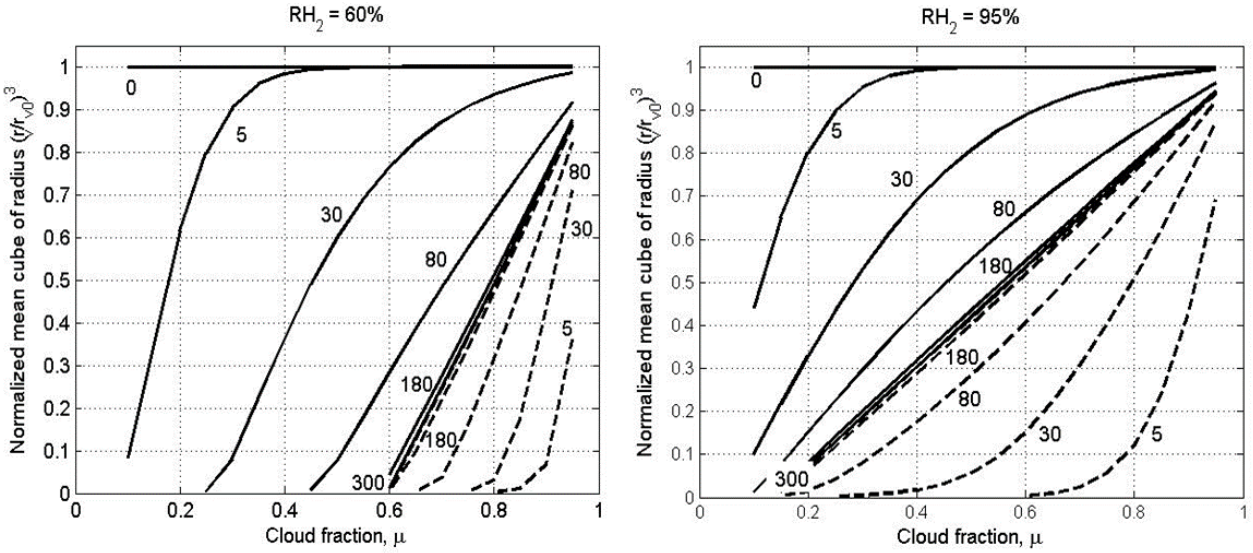

Fig. 8. Dependences of normalized cube of the mean volume radius on the cloud fraction at different time instances for $x = 0$ (solid lines) corresponding to the initially cloud volume, and $x = L$ (dash line) corresponding to the initially dry volume. The time instances in seconds are marked by numbers. The figure is plotted for the narrow initial DSD for two values of RH_2: 60% (left panel) and 95% (right panel). Parameters of DSD are given in Tab. 1. The initial mixing parameters are $T = 10^{\circ}C$, $p = 828.8$ mb and $L = 40$ m. Calculations performed within the range of $0.1 < \mu < 0.95$.

997

998

999

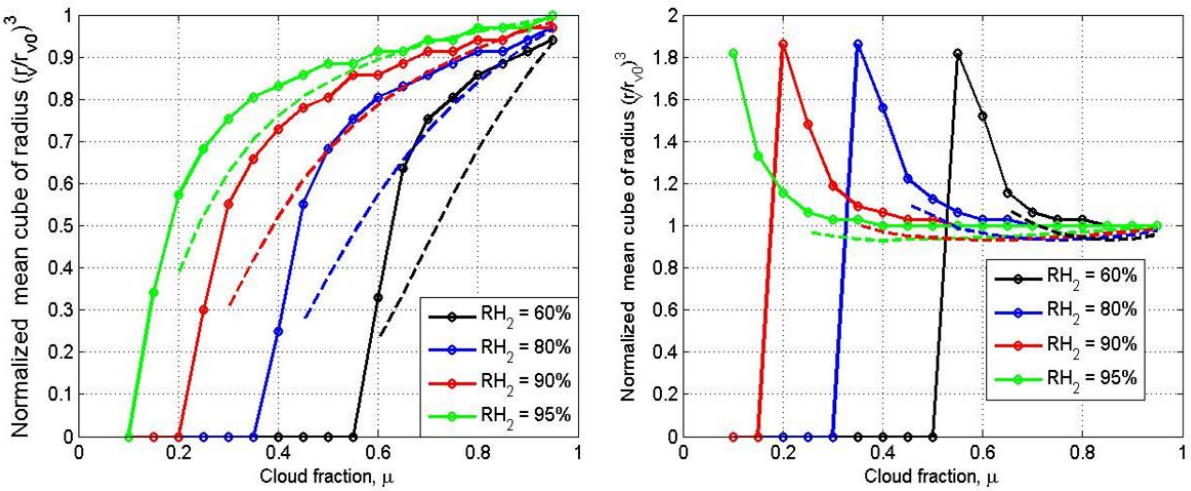

1000

1001

1002

1003 **Fig. 9.** Mixing diagrams. Normalized cube of the mean volume radius vs. the cloud
1004 fraction for initial narrow DSD (left) and initial wide DSD (right). The dependencies
1005 correspond to the equilibrium state. Parameters of initial DSD are presented in Tab. 1. Solid
1006 and dashed lines show the mixing diagrams for inhomogeneous and homogeneous mixing,
1007 respectively. The initial mixing parameters are $T = 10\,^{o}C$, $p = 828.8$ mb and $L = 40$ m.

1008

1009

1010

1011

1012

1013

1014

1015

1016

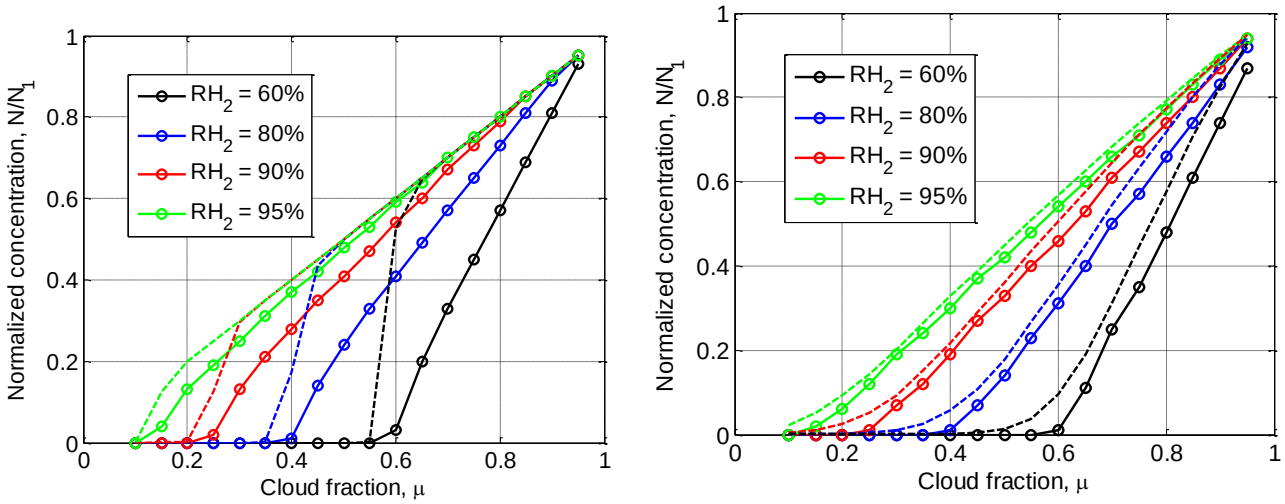

Fig. 10. Final normalized droplet concentration vs. cloud fraction for initially narrow DSD (left) and initially wide DSD (right). Parameters of initial DSD are shown in Tab. 1. Dashed line shows the results of equivalent homogeneous mixing. The initial mixing parameters are $T = 10\,^{o}C$, $p = 828.8$ mb and $L = 40$ m.

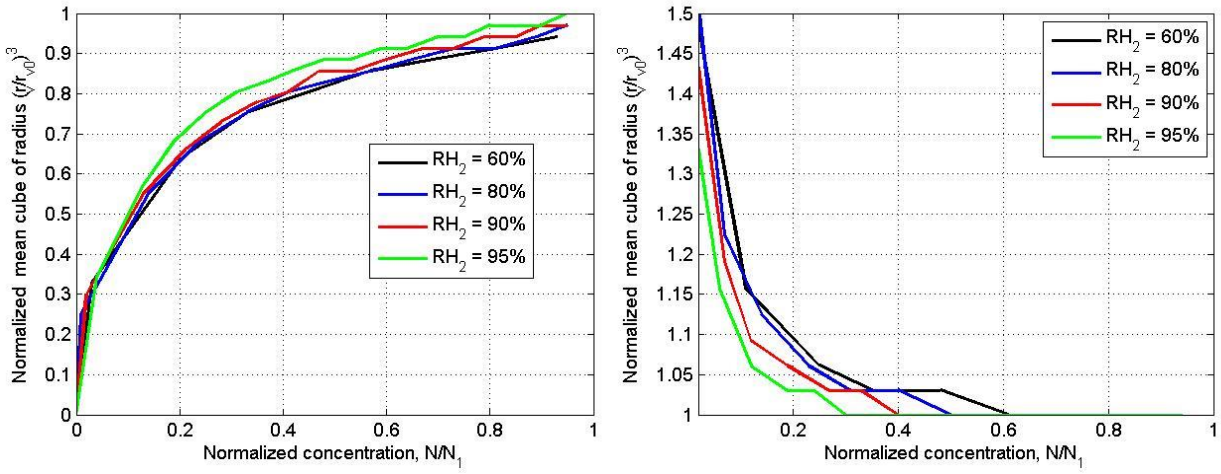

Fig. 11. Dependencies of normalized cube of the effective radius on normalized droplet concentration for different initial relative humidity values. Left panel: narrow initial DSD. Right panel: wide initial DSD. The initial mixing parameters are $T = 10^{\circ}C$, $p = 828.8$ mb and $L = 40$ m.